Angle Diversity for Nondirected Wireless Infrared Communication

Jeffrey B. Carruthers, *Member, IEEE,* and Joseph M. Kahn, *Fellow, IEEE*

***Abstract*—We outline the benefits and challenges of using angle diversity in nondirected wireless infrared (IR) communications systems. Multiple transmitter beams and multiple narrow field-of-view receivers reduce the path loss, multipath distortion, and background noise of the channel, which leads to improved range. We also discuss practical considerations for multielement angle-diversity systems, including channel characterization and suboptimal detection techniques. Maximal-ratio combining provides nearly optimal performance up to 100 Mb/s for the angle-diversity systems considered. The design and performance of a prototype angle-diversity IR communication system are discussed. The prototype can maintain 70 Mb/s at a P_e of 10^{-9} over a 4-m range.**

***Index Terms*—Optical communication, wireless LAN.**

I. Introduction

HIGH-SPEED wireless communication inside buildings can be achieved using nondirected infrared (IR) links [1]. Nondirected links, which consist of wide-beam transmitters and wide field-of-view (FOV) receivers, eliminate the need to point the transmitter and receiver at each other. Such links are made more robust if they are designed to use non line-of-sight (LOS) paths (via illumination of the ceiling or walls) instead of, or in addition to, the LOS path [1], [2].

The conventional approach to nondirected IR links is depicted in Fig. 1(a). A detector with a wide FOV collects unwanted ambient light along with the desired signal. Steady light sources, such as the sun and incandescent lamps, lead to white, nearly Gaussian shot noise; modulated light sources, such as fluorescents, give rise to cyclostationary noise. Also, a wide FOV receiver collects not only the primary illuminated spot, but also signals that have undergone two or more reflections, and are thus delayed. This process, while increasing the collected signal power, introduces multipath distortion.

We consider the use of a multibeam transmitter and multiple nonimaging receivers [3]–[5]. As shown in Fig. 1(b), a detector array of narrow FOV detectors, which together cover the same FOV as a single, wide FOV detector, can reject ambient light that does not coincide with the signal. Further, the multipath distortion is reduced since a smaller fraction of the delayed light lies within the same FOV as the primary signal. The use of multiple beams reduces path loss as compared to a single wide-beam transmitter [5], and is particularly effective when combined with narrow FOV receivers since these receivers can then collect the concentrated signal while rejecting the more diffused noise

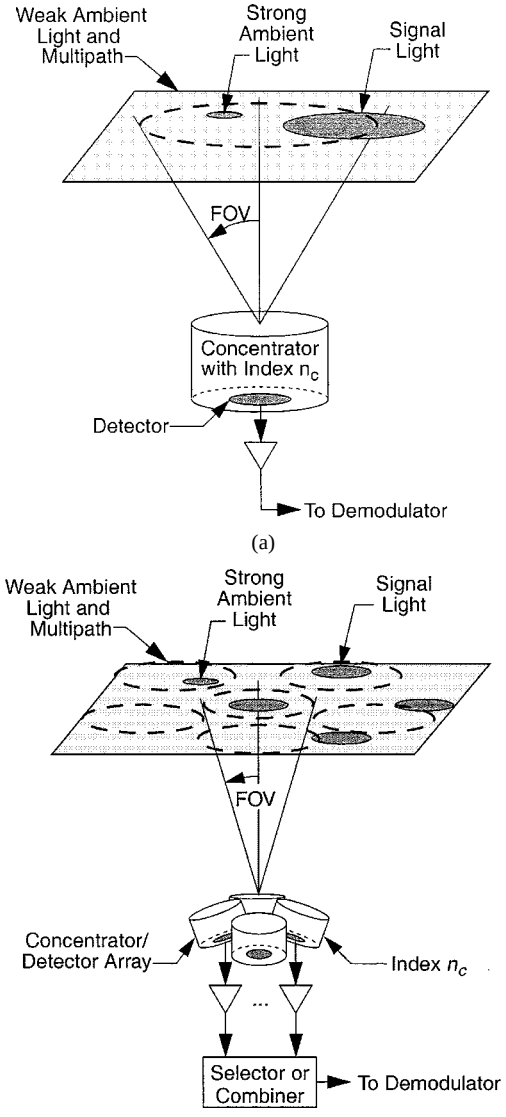

Fig. 1. Two types of nondirected IR links: (a) a wide FOV receiver with large signal spot and (b) an array of narrower FOV detectors and multiple signal spots. Multiple narrow FOV receivers cover a wide FOV but reject ambient light that does not coincide with the signal, and reduce multipath distortion since most of the delayed light from multiple bounces will not coincide with the primary signal. Multiple transmit beams reduce path loss and increase signal-to-noise ratio (SNR) by concentrating the signal within a single receiving element.

Paper approved by J. J. O'Reilly, the Editor for Optical Communications of the IEEE Communications Society. Manuscript received August 15, 1997; revised March 15, 1999 and October 15, 1999. This work was supported by the National Science Foundation under Grant ECS-9710065 and Grant ECS-9876149. This paper was presented in part at ICC'98, Atlanta, GA, 1998.

J. B. Carruthers is with the Department of Electrical and Computer Engineering, Boston University, Boston, MA 02215 USA.

J. M. Kahn is with the Department of Electrical Engineering and Computer Sciences, University of California at Berkeley, Berkeley, CA 94720 USA.

Publisher Item Identifier S 0090-6778(00)05391-5.

sources. Our goals are to characterize the effect of multipath distortion and noise on high-speed IR links, to examine transmitter and receiver design using practical optical and optoelectronic techniques, to demonstrate with an experimental system the effectiveness of angle-diversity IR systems, and to explore related implementation issues.

In Section II, we outline both optimal signal detection and potential suboptimal alternatives. In Section III, we examine the effect of transmitter and receiver design on performance and channel characteristics, and evaluate signal detection choices. Section IV describes the design, implementation, and performance of a prototype angle-diversity communication system. Conclusions are presented in Section V.

II. Signal Detection and Combining

The transmitted signal $X(t)$ is transmitted on I channels, using binary pulse-amplitude modulation (PAM) on a pulse $g_{tx}(t)$. The impulse response of channel i is $b_i(t)$, which includes the responsivity factor and the time response of the photodetector. The data is a sequence of L symbols $a[l]$, the symbol interval is T, and the received signal is of the form

$$y_i(t) = \sum_{l=1}^{L} a[l] h_i(t - lT) + N_i(t) \tag{1}$$

where $h_i(t)$ is the convolution of $g_{tx}(t)$ with $b_i(t)$. Assuming the symbols 0 and A are transmitted with equal probabilities, the average transmitted power P_{tx} is $(A/2T) \int g_{tx}(t)\,dt$. Here, $N_i(t)$ is a zero-mean stationary Gaussian noise process with a power spectral density (PSD) $S_{N_i}(j\omega)$. The processes $N_i(t)$ and $N_j(t)$ are jointly independent for all $i \neq j$. This model is applicable to intensity-modulation direct-detection systems.

A. Maximum-Likelihood Detection

In this section, we describe how to obtain a single sequence $x[k]$ that are sufficient statistics for maximum-likelihood sequence detection (MLSD) of $a[k]$ [6]. Define the whitening filter $w_i(t)$ to be the inverse Fourier transform of $1/S_{N_i}^{1/2}(j\omega)$, where we assume that $N_i(j\omega)$ is strictly positive everywhere, and the matched filter is $\hat{h}_i(-t) = h_i(-t) * w_i(-t)$. Applying $w_i(t) * \hat{h}(-t)$ to each channel reception $y_i(t)$, summing, and baud-rate sampling yields the sufficient statistic $v[k]$ [7]

$$v[k] = \left(\sum_{i=1}^{I} y_i(t) * w_i(t) * \hat{h}_i(-t) \right) \Bigg|_{t=kT} \tag{2}$$

and by defining

$$f[k] = \sum_{i=1}^{I} \left(h_i(t) * w_i(t) * h_i(-t) * w_i(-t)|_{t=kT} \right) \tag{3}$$

we can arrive at the equivalent discrete-time representation

$$v[k] = \sum_{l} a[k-l] f[l] + \nu[k]. \tag{4}$$

We note that the noise $\nu[k]$ is not white, i.e., $S_\nu(z) = F(z)$. We will refer to the process of generating $v[k]$ as *matched-filter combining* (MFC).

We find a spectral factorization of $S_\nu(z)$, i.e., $S_\nu(z) = (1/\sigma^2)C(z)C^*(1/z^*)$, where $C(z)$ is chosen to be monic, minimum phase, and causal, and we apply the noise-whitening filter $\sigma^2/C^*(1/z^*)$ to the sequence $v[k]$ to obtain a more useful sufficient statistic $x[k]$. We can write

$$x[k] = \sum_{l=0}^{\infty} c[l] a[k-l] + \eta[k] \tag{5}$$

where $c[k]$ are determined by $C(z) = \sum_{k=0}^{\infty} c[k] z^{-k}$, $c[0] = 1$ by construction, and $\eta[k]$ is white with variance σ^2. Given the sequence $x[k]$, the optimal detector performs MLSD to estimate $a[k]$. At high SNR, the error probability of MLSD is given approximately by $P_e \approx CQ(d_{\min}/2\sigma)$, where C is an error coefficient that is usually of order unity [8]. The squared minimum distance is given by

$$d_{\min}^2 = \min_{\{\epsilon_k,\, 1 \le k \le L\}} \sum_{m=1}^{\infty} \left| \sum_{k=1}^{L} \epsilon_k c[m-k] \right|^2 \tag{6}$$

where $\{\epsilon_k,\, 1 \le k \le L\}$ is a nonzero sequence of error symbols $\epsilon_k = a^{(1)}[k] - a^{(2)}[k]$.

B. Combining and Equalization

We consider simple alternatives to both MFC and MLSD with the goal being to provide near-optimal performance with techniques that are practical to implement. We will consider selection combining (SC), equal-gain combining (EGC), maximal-ratio combining (MRC), and minimum mean-square-error combining (MMSE) as alternatives to MFC. Unequalized threshold detection and zero-forcing decision-feedback equalization (ZF-DFE) will be discussed as alternatives to MLSD.

In MFC, we apply a filter $\gamma_i(t) = w_i(t) * \hat{h}_i(-t)$ to each channel reception, and then sum the outputs. For SC and MRC, we replace this filter bank with a combiner, i.e., a bank of gains W_i followed by a summer, and apply a common filter $\gamma(t)$. The result is an effective receiver filter for channel i of $\gamma_i(t) = W_i \gamma(t)$. In EGC, the W_i are equal to some constant.

We will use a five-pole low-pass Bessel filter for $\gamma(t)$, and use cutoff frequencies that are appropriate for the data rate used and for the detection method employed.

The resulting equivalent discrete-time system is given by (4), where

$$f[k] = \sum_{i=1}^{I} W_i f_i[k], \qquad f_i[k] = h_i(t) * \gamma(t)|_{t=kT} \tag{7}$$

and

$$\begin{aligned} S_\nu(z) &= \sum_{i=1}^{I} W_i^2 S_{\nu_i}(z) \\ S_{\nu_i}(e^{j\omega T}) &= \frac{1}{T} \sum_{m=-\infty}^{\infty} \left(S_{N_i}(j(\omega + 2\pi m/T)) \right) \\ &\quad \cdot |\Gamma(j(\omega + 2\pi m/T))|^2. \end{aligned} \tag{8}$$

Here, $\Gamma(j\omega)$ is the Fourier transform of $\gamma(t)$.

We define the signal-to-noise ratio SNR_i of channel i and the SNR of the combined channel to be

$$\mathrm{SNR}_i = \frac{P_{tx}^2 B_i^2(0)\Gamma_i^2(0)}{\int S_{N_i}(j\omega)\,|\Gamma(j\omega)|^2\,d\omega} \tag{9}$$

$$\mathrm{SNR} = \frac{P_{tx}^2\left(\sum_i B_i^2(0)\Gamma_i(0)\right)^2}{\sum_i \int S_{N_i}(j\omega)\,|\Gamma(j\omega)|^2\,d\omega}. \tag{10}$$

When $\gamma_i(t) = W_i\gamma(t)$, then these simplify to

$$\mathrm{SNR}_i = \frac{P_{tx}^2\Gamma^2(0)B_i^2(0)}{\int S_{N_i}(j\omega)\,|\Gamma(j\omega)|^2\,d\omega} \tag{11}$$

$$\mathrm{SNR} = \frac{P_{tx}^2\Gamma^2(0)\left(\sum_i W_i B_i(0)\right)^2}{\sum\left[W_i^2\left(\int S_{N_i}(j\omega)\,|\Gamma(j\omega)|^2\,d\omega\right)\right]}. \tag{12}$$

We have incorporated the receive filter $\gamma(t)$ so that the SNR is considered in the traditional way in the SC and MRC algorithms, and so that the effects of nonwhite noise are correctly accounted for. On an ideal channel with $b_i(t) = B_i(0)\delta(t)$ and additive white Gaussian noise with two-sided PSD N_0, the optimal choice of γ would be $\mathrm{rect}(t, T/2)$, a filter with rectangular impulse response of width T, and the probability of bit error P_e is $Q(\sqrt{\mathrm{SNR}})$. Then we would have $\mathrm{SNR} = P_{tx}^2 B_i^2(0)T/N_0$, or recalling that $R_b = 1/T$, $\mathrm{SNR} = P_{tx}^2 B_i^2(0)/(R_b N_0)$ as in [1].

MRC maximizes the SNR over all possible choices of W_i (to within a scale factor) and the maximizing weights are

$$W_i = \frac{B_i(0)}{\int S_{N_i}(j\omega)\,|\Gamma(j\omega)|^2\,d\omega}. \tag{13}$$

Hence

$$\mathrm{SNR}_{\mathrm{MRC}} = \sum_i \frac{P_{tx}^2\Gamma^2(0)B_i^2(0)}{\int S_{N_i}(j\omega)\,|\Gamma(j\omega)|^2\,d\omega} = \sum_i \mathrm{SNR}_i. \tag{14}$$

The MMSE combiner is the vector $W = [W_i]$, $i = 1, \cdots, I$, that minimizes the expectation of

$$\epsilon_k^2 = \left(d[k] - \sum W_i f_i[k]\right)^2 \tag{15}$$

where $d[k] = 2a[k]/A - 1$. The solution is $W = R^{-1}P$ and

$$R = [R_{ij}], \qquad R_{ij} = \sum_l f_i[l]f_j[l] + \rho_{\nu_i}[0]\delta_{ij} \tag{16}$$

$$P = [P_i], \qquad P_i = f_i[0]. \tag{17}$$

Here, $\rho_{\nu_i}[k]$ is the inverse z-transform of $S_{\nu_i}(z)$.

When linear memoryless combining or MFC is employed, the error probability of unequalized detection of on–off keying (OOK) is given by [9]

$$P_e = \sum_{\substack{a[k]\in\{0,1\}\\ k=1,\cdots,K}} \frac{1}{2^K} \cdot Q\left(\frac{A}{2\sqrt{\rho_\nu[0]}}\left(\sum_{k=0}^{K}\hat{f}[k] - 2\sum_{k=1}^{K}a[k]\hat{f}[k]\right)\right) \tag{18}$$

where $\rho_\nu[k]$ is the inverse z-transform of $S_\nu(z)$, $\hat{f}[0]$ is the largest element of $f[k]$, and $\hat{f}[k]$, $k = 1, \cdots, K$ are the remaining nonzero elements in $f[k]$. By construction, the sequence $\hat{f}[k]$ is causal, although the original sequence $f[k]$ is not necessarily so. In general, $f[k]$ is of infinite extent, but in practical cases, we can truncate it after tap K. For the purpose of computing (18), it is more efficient to select the K taps with the largest amplitudes rather than a block of K contiguous taps.

The probability of error of a symbol-rate infinite-length ZF-DFE [8] is given by $P_e = Q(\sqrt{A^2/(4\varepsilon^2)})$, where ε^2 is the geometric mean of $S_\nu/|F|^2$ and we assume no errors in the feedback path, which will be a very good approximation in the low P_e region of interest.

III. Transmitter and Receiver Design

We wish to quantify the potential advantages of using multiple narrow-beam transmitters and multiple, narrow FOV receivers, namely, elimination of noise sources and multipath. We consider two categories of link configurations: vertically oriented systems that rely on reflections from the ceiling and other surfaces, and horizontally oriented systems that primarily rely on an LOS path between at least one transmit beam and one receiver element.

We consider transmitters with generalized Lambertian radiation patterns of order N, where the transmit power per steradian $R(\phi)$ at an angle ϕ from the normal is given by

$$R(\phi) = P\,\frac{(N+1)}{2\pi}\,\cos^N(\phi)\,\mathrm{rect}(\phi, \pi/2) \tag{19}$$

and P is the total power. Such beams can be generated using diffusers or more efficiently with computer-generated holograms [1].

The receivers use ideal optical concentrators [10], which provide optical gain at the expense of a narrower FOV. The effective area at an angle θ of an optical detector of area A_{det} with an ideal optical concentrator of refractive index n and cutoff angle θ_c is given by

$$A(\theta) = \frac{n^2 A_{\mathrm{det}}}{\sin^2(\theta_c)}\,\cos(\theta)\,\mathrm{rect}(\theta, \theta_c). \tag{20}$$

One implementation of a nearly ideal optical concentrator is a compound-parabolic concentrator (CPC), which provides an effective area at an angle θ that is well modeled [11] by

$$A(\theta) = \frac{n^2 A_{\mathrm{det}}}{\sin^2(\theta_c)}\,\frac{\cos(\theta)T}{1 + (\theta/\theta_c)^{2R}} \tag{21}$$

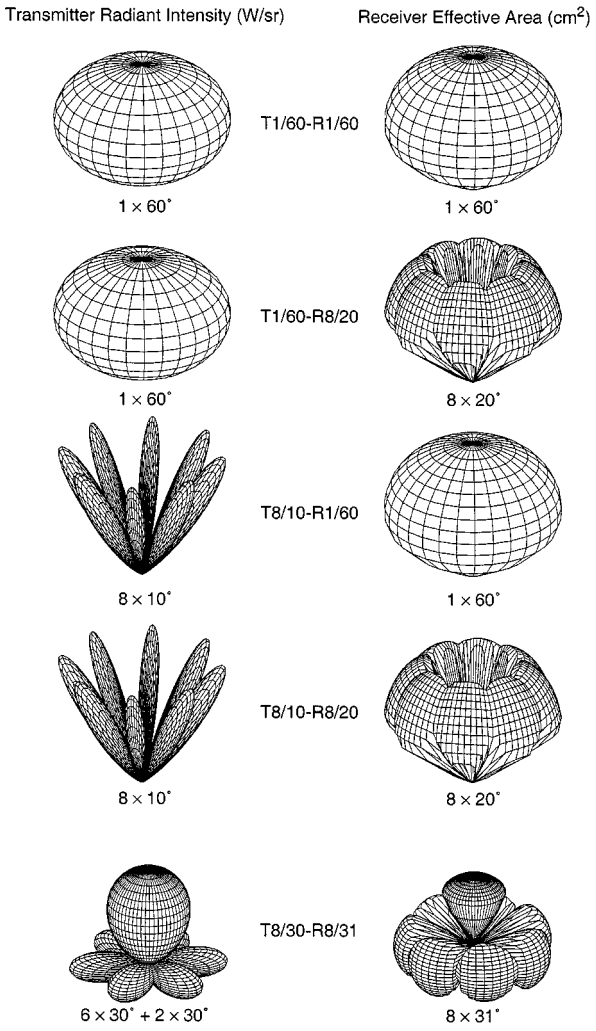

Fig. 2. Transmitter radiant intensity and receiver effective area for four vertically oriented links and one horizontally oriented link.

where $T > 0.9$ and $R = 13$. We denote the total detector area of the receiver by $A_{\rm tot}$ and the area of a particular detector by $A_{\rm det}$. Throughout this section, $A_{\rm tot} = 1$ cm^2 and the refractive index of the optical concentrator is $n_c = 1.44$. The total transmit power P_{tx} is 0.6 W.

The most important systems under consideration are shown in Fig. 2, which show the radiation pattern of the transmitter in watts per steradian and the effective area of the receiver as a function of angle. There are four vertically oriented systems shown and one horizontally oriented system. For the vertical systems, we consider two options for the transmitter. The first (T1/60) has a first-order Lambertian radiation pattern and is pointed directly at the ceiling. It has average transmitted optical power P_{tx} and a half-power semiangle (HPSA) of 60°. The second (T8/10) uses eight separate narrow beams with 37° elevation from horizontal and 45° azimuthal separation angles. They are modeled as generalized Lambertian-pattern transmitters with HPSA of 10°. The average transmitted optical power of each beam is $P_{tx}/8$. We also consider two options for the receiver. The first (R1/60) is a p-i-n photodetector with area $A_{\rm tot}$ and an ideal nonimaging optical concentrator with 60° cutoff angle, refractive index n_c, and an optical filter of bandwidth $\Delta\lambda$. The second receiver (R8/20) uses an array of eight p-i-n photodetectors, each with area $A_{\rm tot}/8$ and ideal 20° nonimaging optical concentrators with the same refractive index and optical-filter bandwidths as for the single receiver. They are oriented with 45° elevation angles and 45° azimuthal separation angles. We will refer to the four different configurations of transmit/receive pairings as T1/60-R1/60, T1/60-R8/20, T8/10-R1/60, and T8/10-R8/20, respectively.

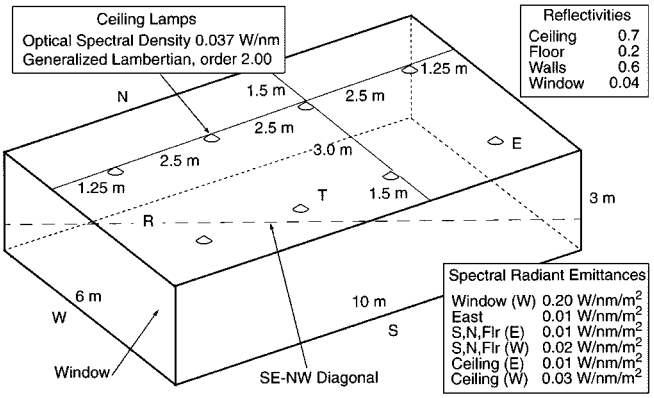

Fig. 3. Room model for analysis of transmitter and receiver configurations. The west wall is a single large window. We model the walls, ceiling, floor, and window as Lambertian reflectors which also act as ambient light sources. The ceiling lamps are 100-W floodlights. The location of the transmitter is indicated by a "T." The southeast to northwest diagonal is the location of the receiver in Figs. 4, 5, and 7.

The best performing horizontal system is also shown in Fig. 2. This system (T8/30-R8/31) uses six equal-power 30° HPSA transmit beams equally spaced in the horizontal plane. In addition, two such beams are pointed straight up to provide connectivity when the vertical separation of the transmitter and receiver is such that the LOS link is not present. The receiver (R8/31) uses eight 31° optical concentrators, seven of which are horizontally oriented and the last pointed up. The horizontal receiver elements must have significant overlap in their FOV in the horizontal plane because of the sharp cutoff in their directivity. Although there are a total of 20 possible pairings of the 5 transmitters and 4 receivers considered, we have considered only 5 pairings. The other 15 possibilities either have obviously mismatched characteristics of transmitter and receiver or were tested and shown to have consistently poorer performance than a similar pairing.

A. Modeling Rooms: Surfaces and Noise Sources

To evaluate the effect of the transmitter and receiver design on multipath mitigation, we consider a room representative of a medium-sized open office, shown in Fig. 3. It is 6 m (east to west) by 10 m (north to south) with 3-m ceilings, where the west wall is a single large window. We assume that the signal source has a center wavelength of 806 nm and that optical filters are employed that effectively block all light outside of the range 780–830 nm. The source linewidth is insignificant relative to the bandwidth of the optical filters.

We model the walls, ceiling, floor, and window[1] as Lambertian reflectors of reflectivities 0.6, 0.7, 0.2, and 0.04, respectively. Further, these surfaces act as ambient light (noise) sources. They are modeled as planar Lambertian transmitters with emissions as shown in Fig. 3, based on measurement data [7]. We also include eight ceiling 100-W tungsten floodlights, positioned as shown in Fig. 3. Measurements of these lamps [7] show that an excellent model for their radiant intensities is a generalized Lambertian [1] pattern of order $n_{\text{lamp}} = 2.0$ with optical spectral density of $p_{\text{lamp}} = 0.037$ W/nm.

The background-light induced shot noise has double-sided PSD $S_{\text{shot}} = qA_{\text{det}}Ri_{\text{bg}}$ where $R = 0.6$ A/W and i_{bg} is the irradiance of the background light on the detector surface. We calculate i_{bg} according to

$$i_{\text{bg}} = \sum_{\text{six surfaces } C_i} \left(\int_{C_i} \Delta\lambda\, S_i(x, y)\, \frac{\cos\left(\phi_i(x, y, \vec{R})\right)}{\pi d^2(x, y, \vec{R})} \cdot \frac{A\left(\theta_i(x, y, \vec{R})\right)}{A_{\text{det}}}\, dx\, dy \right) + \sum_{\text{lamp } j} \Delta\lambda\, p_{\text{lamp}}\, \frac{(n_{\text{lamp}} + 1)}{2\pi} \cdot \frac{\cos^{n_{\text{lamp}}}\left(\phi_j(\vec{L}_j, \vec{R})\right)}{d^2(\vec{L}_j, \vec{R})}\, \frac{A\left(\theta_j(\vec{L}_j, \vec{R})\right)}{A_{\text{det}}} \tag{22}$$

where $S_i(x, y)$ is the spectral radiant emittance at (x, y) of surface i, ϕ_i is the angle between the normal of the emitter i and the receiver-emitter line, θ_i is the angle between the normal of the detector and the emitter-detector line, $\vec{R}$ is a five-tuple representing the position and orientation of the receiver, $\vec{L}_j$ is a five-tuple representing the position and orientation of lamp point noise source j, $d(\cdot)$ is the distance between receiver and source, and the function $A(\theta)$ is given by (20).

We must take into account, in addition to the background noise sources, the receiver noise spectrum with photodiode capacitance appropriately accounted for. We assume a transimpedance preamplifier with a bipolar junction transistor in the first stage, and the capacitance of the photodiode is $C_{\text{det}} = A_{\text{det}}c_{src}$ where $c_{src} = 30$ pF/cm^2. We model the double-sided PSD of the thermal noise in each receiver as [7]

$$S_{rx}(f) = 2kT/R_f + qI_b + 2kT(2\pi f)^2 \left[C_{\text{det}}^2 R_{\text{base}} + (C_{\text{det}} + C_\pi)^2 \left(1/(2g_m) + 1/(R_c g_m^2)\right) \right] \tag{23}$$

where $I_b = 19.5\ \mu$A, $R_f = 2.5$ kΩ, $C_\pi = 1.7$ pF, $R_c = 146\ \Omega$, $R_{\text{base}} = 68\ \Omega$, and $g_m = 70$ mS.

B. Channel Characterization

We evaluate channel impulse responses using the recursive impulse response calculation described in [12], with two extensions, the first allowing for multiple transmit beams and the second allowing for arbitrary receiver gain versus angle characteristics. The first was done by considering each transmit beam separately, and then adding the impulse response from each. The second was done by replacing the $\cos(\theta)$ gain dependence of the receiver with an arbitrary function $g(\theta)$.

[1]Although glass is a specular reflector, we model it as Lambertian reflector for computational simplicity. The resulting error is small since the reflectivity is much less than the other surfaces of the room.

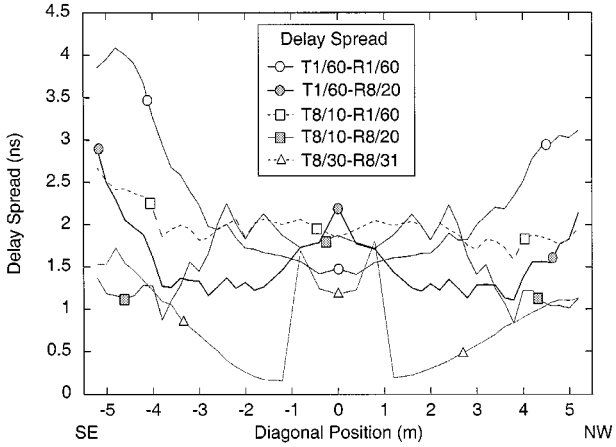

Fig. 4. RMS delay spreads of the MRC-combined channel for four vertically oriented systems and one horizontally oriented system. The receiver locus and transmitter position are shown in Fig. 3; the receiver moves along the southeast $(-)$ to northwest $(+)$ diagonal 1.0 m from the floor, and the transmitter is located in the center of the room 1.5 m from the floor. The 0.6-W transmitter is located in the center of the room 1.5 m from the floor.

A typical set of impulse responses for the four vertically oriented transmitter/receiver configurations were calculated. The transmitter is located in the center of the room at a height of 1.5 m. The receiver is located 3.43 m north and 2.05 m west of the transmitter at a height of 1, which places it 4 m away from the transmitter in the direction of the north-west corner of the room. Both the T1/60-R1/60 and T8/10-R1/60 systems have significant energy in their impulse responses at about 20 ns away from the peak. This spreading is due to multiple reflections from diffuse reflecting surfaces. The impulse responses of the horizontally oriented systems have large LOS components and very little multipath dispersion.

The temporal dispersion of an impulse response $b(t)$ can be expressed by the *channel root-mean-square (rms) delay spread* D. The T1/60-R1/60 configuration had the highest delay spread, 2.5 ns, and lowest SNR, 12.2 dB, of the four configurations considered. Going to a multiple-beam transmitter (T8/10-R1/60) increases the SNR by 3.0 dB and reduces the delay spread to 1.7 ns. The T1/60-R8/20 configuration increases the SNR compared to T1/60-R1/60 by 1.6 dB for SC and by 3.3 dB for MRC. Also, the delay spread of the channel for SC is only 0.9 ns and the delay spread of the composite MRC channel is 1.3 ns. The best performing vertical configuration in terms of both SNR and delay spread is T8/10-R8/20, which achieves an SNR of 15.6 dB for SC and 19.4 dB for MRC. The delay spreads of the horizontal system T8/30-R8/31 are 0.9 ns for SC and 1.2 ns for MRC. The SNR for this system is 19.4 dB.

A better perspective on how delay spread and SNR vary with receiver position within a room is obtained by plotting their values along a diagonal of the room, as is done in Figs. 4 and 5. The transmitter is located in the center of the room at a height of 1.5 m. The diagonal position is the horizontal distance from the receiver to the transmitter along the southeast

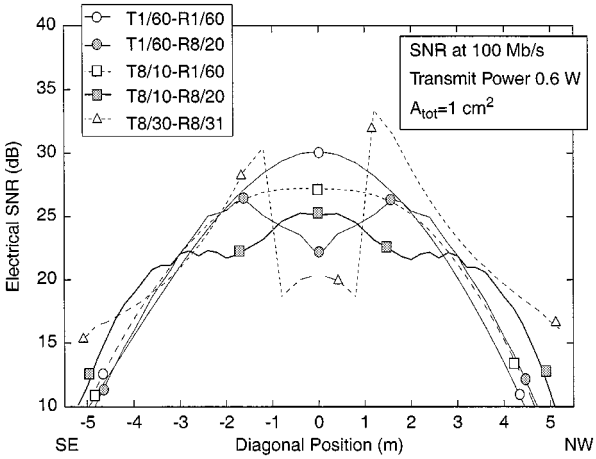

Fig. 5. SNR of the MRC-combined channel for the same conditions as Fig. 4. 100-Mb/s OOK is employed.

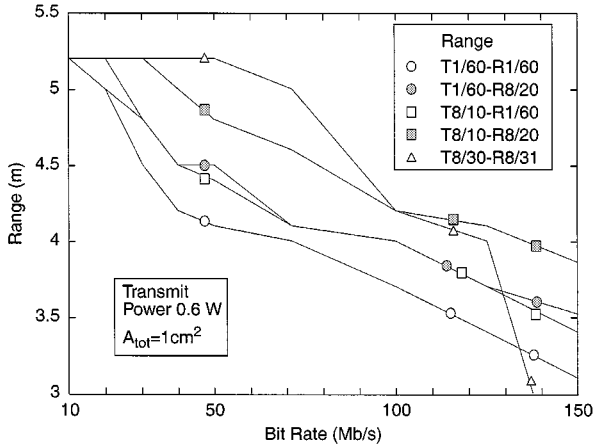

Fig. 6. Range at $P_e = 10^{-9}$ for MFC-MLSD of four vertically oriented systems and one horizontally oriented system. The 0.6-W transmitter is located in the center of the room shown in Fig. 3, is 1.5 m from the floor, and is sending 100-Mb/s OOK.

to northwest diagonal, and the delay spread is the rms delay spread of the MRC-combined channel. The single-receiver systems exhibit a general increase in delay spread as the receiver moves away from the transmitter to the edge of the room. The multiple-element receivers have lower MRC-combined channel delay spreads than the single channel of single-element receivers, especially further away from the transmitter. This is especially important due to the trend of decreasing SNR shown in Fig. 5. Also, the multiple-element receivers exhibit less east-west asymmetry in delay spread due to the low reflectivity of the window; for the R8/20 receiver, this is because the MRC-combined channel is dominated by light reflected from the ceiling, and for the R8/31 and R8/40 receivers, it is because the MRC-combined channel is dominated by the LOS path.

The sudden drop in delay spread of the MRC-combined channel of the horizontal system at diagonal positions near 1 m is best explained in conjunction with the SNR curve of Fig. 5. The T8/30-R8/31 system loses its LOS link at horizontal separations of less than 1 m due to the 0.5-m height difference in the locations of transmitter and receiver, resulting in a 10-dB SNR drop. This explains the necessity to have some vertically oriented transmit and receive elements even for horizontally oriented systems. The effect of the increased noise from the window has opposite effects on horizontal and vertical systems. The vertical systems exhibit decreases in SNR near the window relative to the far side of the room, but the SNR of the horizontal systems increase. This is because in the horizontal systems, the signal and the increased noise are on opposite sides of the receiver, and hence go to different receivers when the receiver is near the window. When the receiver is in the southeast corner, the horizontal receiving elements with a view of the transmitter are also pointing at the window and so the SNR is reduced. The ceiling-oriented multiple receiver (R8/20) exhibits the least effect from the window. The SNR is slightly degraded on the window side due to the increase ambient noise from the ceiling and walls on the west side of the room.

C. Range and Error Performance

Previous work [2], [13] has lead to the conclusion that the P_e performance of nondirected IR channels can be predicted by the SNR and delay spread. The power penalty due to ISI is defined in this multiple-channel case as the additional power required to achieve $P_e = 10^{-9}$ for the channels $b_i(t)$, suitably combined, relative to the power required for the channels $B_i(0)\delta(t)$, i.e., the ISI-free channels with the same optical gain.

The expected relationship between power penalty of OOK (unequalized and ZF-DFE) and the rms delay spread of the MRC-combined channel for the vertical systems holds. Hence, the power penalties agree with each other and the ceiling-bounce model developed in [13]. Although the horizontally oriented systems show a general increase in power penalty with delay spread, the power penalty scatter is quite large and the values do not coincide with the vertical systems or the ceiling-bounce model.

We look at two measures of error performance: range and power margin. Range is defined as the horizontal distance the receiver can lie from the transmitter in any direction while still achieving a P_e of 10^{-9}. Power margin is the excess transmit power for achieving the goal of $P_e = 10^{-9}$; a negative power margin in decibels indicates one needs additional power to achieve $P_e = 10^{-9}$.

The range as a function of the data rate is depicted in Fig. 6 for MFC-MLSD. At data rates of 10 Mb/s and less, all of the systems surpassed $P_e = 10^{-9}$ throughout the room and so achieved a range of 5.2 m. The T8/30-R8/31 system achieves the largest range for data rates between 30–90 Mb/s, and the T8/10-R8/20 system achieves the largest range at speeds greater than 90 Mb/s. The advantage of spreading the light on the ceiling can be seen by comparing the range of the T8/10-R1/60 system to the T1/60-R1/60 system, and the advantage of multiple receiving elements (at high bit rates) can be seen by comparing the range of the T1/60-R8/20 system to the T1/60-R1/60 system.

The power margin for OOK at 100 Mb/s using MFC-MLSD detection is plotted in Fig. 7 for the southeast to northwest diagonal. The power margin curves are similar to the SNR curves along the same diagonal; the differences are due to the differing multipath characteristics. The T1/60-R8/20 and T8/10-R8/20 systems show better power margin performance relative to others than one would predict from the SNR curves. The

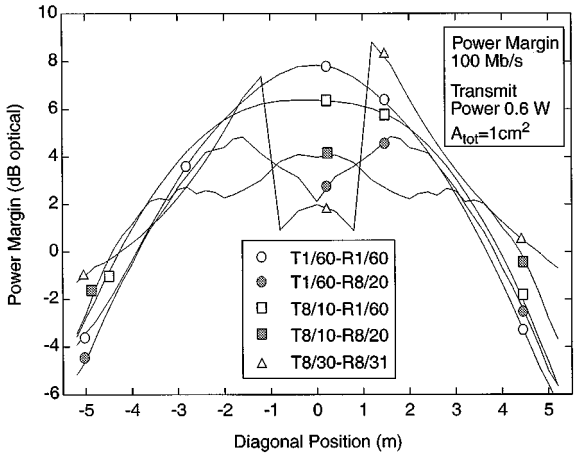

Fig. 7. Power margin at $P_e = 10^{-9}$ for MFC-MLSD of the T1/60-R1/60, T8/10-R1/60, T1/60-R8/20, T8/10-R8/20, and T8/30-R8/31 systems in the room shown in Fig. 3, along the southeast to northwest diagonal. The 0.6-W transmitter is located in the center of the room 1.5 m from the floor, and is sending 100-Mb/s OOK.

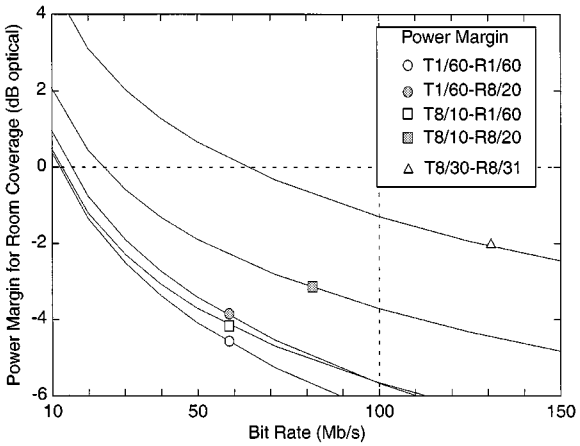

Fig. 8. Power margin at $P_e = 10^{-9}$ for covering the room shown in Fig. 3 with a 0.6-W transmitter, which is located in the center of the room 1.5 m from the floor. OOK with MFC-MLSD is employed. "Room coverage" is defined for receiver locations over the center 90% of the room in a plane 1.0 m above the floor.

same asymmetry properties that appeared in the SNR curves are present in the power margin along the diagonal. One can get insight on why the range at 100 Mb/s is best for the T8/10-R8/20 system from this graph. Although on the northwest diagonal, the T8/30-R8/31 system has a better margin and on the southeast diagonal, the T8/10-R1/60 system has a better power margin, the T8/10-R8/20 system achieves the highest "range" on the diagonal. Of course, the true range is the minimum over all such rotational slices of the power margin surface, and so the range along the diagonal will be greater than the true range.

The MFC-MLSD OOK power margin as a function of data rate is plotted in Fig. 8. The power margin is for coverage of the center 90% of the room. By this measure, the horizontal system clearly outperforms the vertical systems—it is at least 2 dB better than any of the vertical systems considered at all data rates between 10–150 Mb/s. The maximum data rate for room coverage for the reference transmit power of 600 mW varies from 12 Mb/s for T1/60-R1/60 to 65 Mb/s for T8/30-R8/31; the T8/10-R8/20 system achieves 25 Mb/s. The significant difference between horizontal systems and vertical systems in power margin can be understood by examining the power margin at the far ends of the northwest diagonal shown in Fig. 7. Not only is the power margin of the horizontal system higher than the vertical systems there, the downward slope is not as extreme.

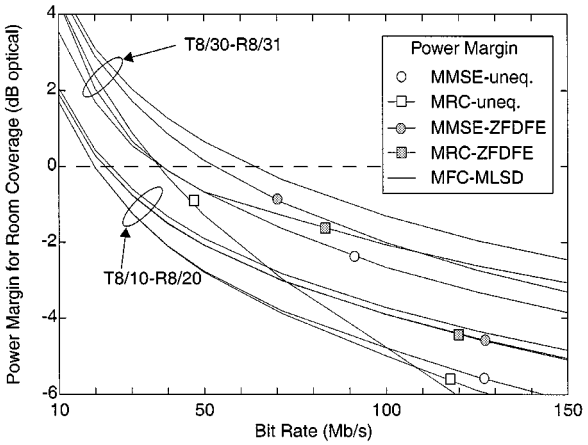

Fig. 9. Power margin at $P_e = 10^{-9}$ for various combining and detection methods of the T8/10-R8/20 and T8/30-R8/31 systems in the room shown in Fig. 3. 100-Mb/s OOK is employed.

One can evaluate the performance of combining and equalization techniques by examining the power margin for room coverage in Fig. 9. The power margin graph shows that MMSE is better than MRC for unequalized operation and high data rates. MMSE and MRC perform similarly when followed by a ZF-DFE. The penalty for employing MRC ZF-DFE instead of MFC-MLSD at 100 Mb/s is 0.2 dB for T8/10-R8/20 and is 0.8 dB for T8/30-R8/31.

IV. A Prototype Angle-Diversity System

We have built a prototype angle-diversity IR communications link that is most similar to the T8/10-R8/20 system considered previously. The system employs nine receiving elements and eight transmit beams. The system was primarily designed to operate and was tested at 70 Mb/s, but it could be operated at transmission rates of 10 Mb/s up to 100 Mb/s. The transmitter sends OOK pulses using intensity modulation and the receiver employs direct detection. The system was tested in the two rooms depicted in Fig. 10. The first is a conference room with large windows on the south and west walls, and the other, a brightly lit optical laboratory.

A. System Design

The transmitter described in [14] was modified to produce eight steerable, collimated beams. The maximum fully modulated average transmitted optical power of each laser is 75 mW, for a resulting total power of 0.6 W. The center wavelengths of the transmit beams vary from 805 to 808 nm and the 10-dB linewidths vary from 2.4 to 3.4 nm. The transmit beams have an elevation angle of 70°, which when aimed at the ceiling produce a ring of eight spots with diameter 1.9 m in Room 400 and 1.1 m in Room 173.

The implementation of a single-receiver element is depicted in Fig. 11(a). The receiver optics consist of an optical filter, a

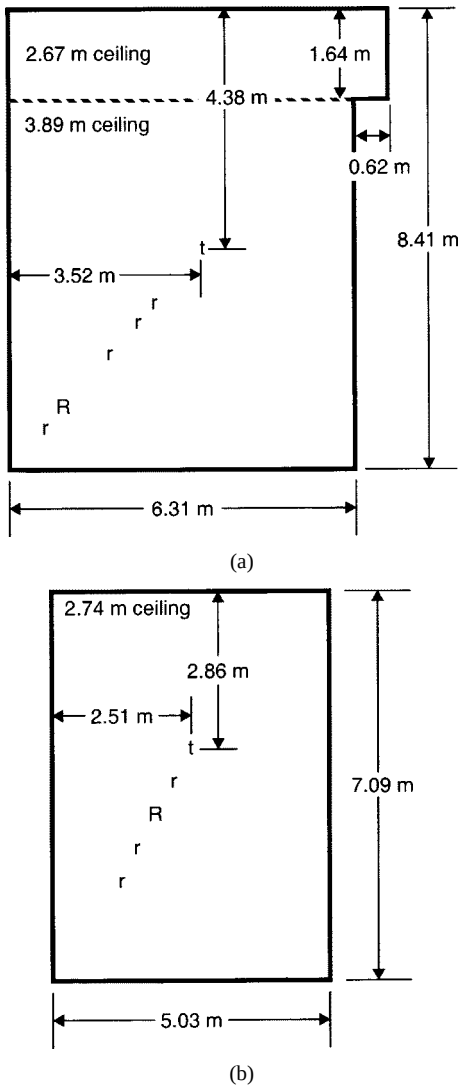

Fig. 10. (a) Room 400, Cory Hall. (b) Room 173, Cory Hall. The transmitter location is indicated by "t" and the receiver locations by "r" or "R."

concentrator, and a photodiode. The optical filter has a nominal center bandwidth of 814.5 nm, a 26-nm half-power bandwidth, a maximum transmission of 0.80, an effective refractive index of 2.0, and provides E-5 blocking (i.e., transmission $T < 10^{-5}$) between 200–1200 nm outside of the passband. The concentrator is a Janos solid CPC with a 19-mm input diameter and 5.0-mm exit diameter made of PMMA, which has refractive index 1.44. It is 45.4 mm long and has cutoff angle $\theta_c = 22°$. The photodetector is an EG&G FFD-200 silicon p-i-n photodiode, n-illuminated with 5.1-mm diameter, 150-MHz bandwidth, and 22-pF capacitance. A reverse bias of -34 V is used. The filter is mounted to the CPC with $n = 1.51$ optical cement, and the CPC is mounted to the photodiode with $n = 1.44$ thermoplastic.[2] The photodiode has a silicon dioxide antireflection coating with a quarter-wave thickness at 830 nm.

The photocurrent is amplified using a 2.5-kΩ transimpedance amplifier based on the Comlinear 425 operational amplifier. The receiver 3-dB bandwidth is 70 MHz, limited by the time constant of the feedback resistor and stabilizing capacitor. Receiver noise is modeled as in (23), except that $c_{src} = 105$ pF/cm^2 for this photodetector, and $A_{\rm det} = 0.21$ cm^2. Hence, the total source capacitance is 24 pF due to the addition of stray capacitance to the detector capacitance. The model predicts a two-sided input-referred current noise density of 2.55 pA/$\sqrt{\rm Hz}$ near DC; the measured values of the nine receivers range from 2.51 pA/$\sqrt{\rm Hz}$ to 2.66 pA/$\sqrt{\rm Hz}$ with a mean of 2.57 pA/$\sqrt{\rm Hz}$. As discussed in [15], one could get better performance by increasing the thickness of the photodiode, thus decreasing its capacitance but at the same time decreasing its bandwidth due to transit-time limitations.

The nine receivers are arranged such that one points vertically toward the ceiling, and the other eight are in a ring with 45° elevation and 45° azimuthal separation angles. The combiner array is implemented using an array of Comlinear 522 variable-gain amplifiers, and the gain of possible tap weights is 0.01–4.1, a 52-dB dynamic range. The combiner array weights are controlled with nine analog voltages in the range -2.1–1.0 V, which are generated using a personal computer analog output board employing a parametric channel estimation technique [7].

Although fluorescent lights do not contribute significantly to shot noise in the receiver, due to their electronic ballasts, they produce periodic interference [16] in the spectrum from 22 kHz to 1.0 MHz. If not mitigated, this interference can cause 2.0-dB optical power penalty in this system when the signal spots are near ceiling fluorescent light fixtures [7]. A 1.6-MHz first-order high-pass filter removes the interference, and quantized feedback (QF) mitigates the baseline wander caused by the filter. The measured penalty from the QF system is 0.2 dB, and when the QF loop is employed, the penalty due to fluorescent light noise is reduced to 0.1 dB. The QF system is depicted in Fig. 11(b).

The detection and error estimation implementation is also shown in Fig. 11(b). We perform unequalized detection using a five-pole low-pass Bessel filter with 35-MHz bandwidth. The error estimate is formed by using a four-quadrant multiplier with differential inputs that subtracts the received signal from the comparator output and squares the result. This squared error is sampled at the eye opening by multiplying with a narrow-pulse clock signal and low-pass filtered with a 2.6-kHz first-order filter. The estimation technique is implemented using a 4-kHz analog-to-digitial sampler.

B. Channel Characterization

The system was tested in the room depicted in Fig. 10(a), a conference room with large windows on the south and west walls. The 3-dB cutoff frequencies of the strongest two channels are 80 and 65 MHz, respectively. The weaker channels have 3-dB cutoff frequencies of about 10 MHz, but since the SNR in these channels is low, the additional multipath in these channels does not affect the overall magnitude response of the combined channel, which has a 75-MHz 3-dB cutoff frequency. The shape of the main lobe of these impulse responses is dominated by the windowing function used to estimate the impulse response from the noisy frequency response. The delay spread of the windowing function is 2.4 ns, so this limits our ability to measure smaller delay spreads. The delay spreads of the two strongest channels are 2.8 and 4.7 ns, respectively. The delay

[2]The optimal refractive index of the thermoplastic is $n = 1.54$ [7]; the $n = 1.44$ material was the best available.

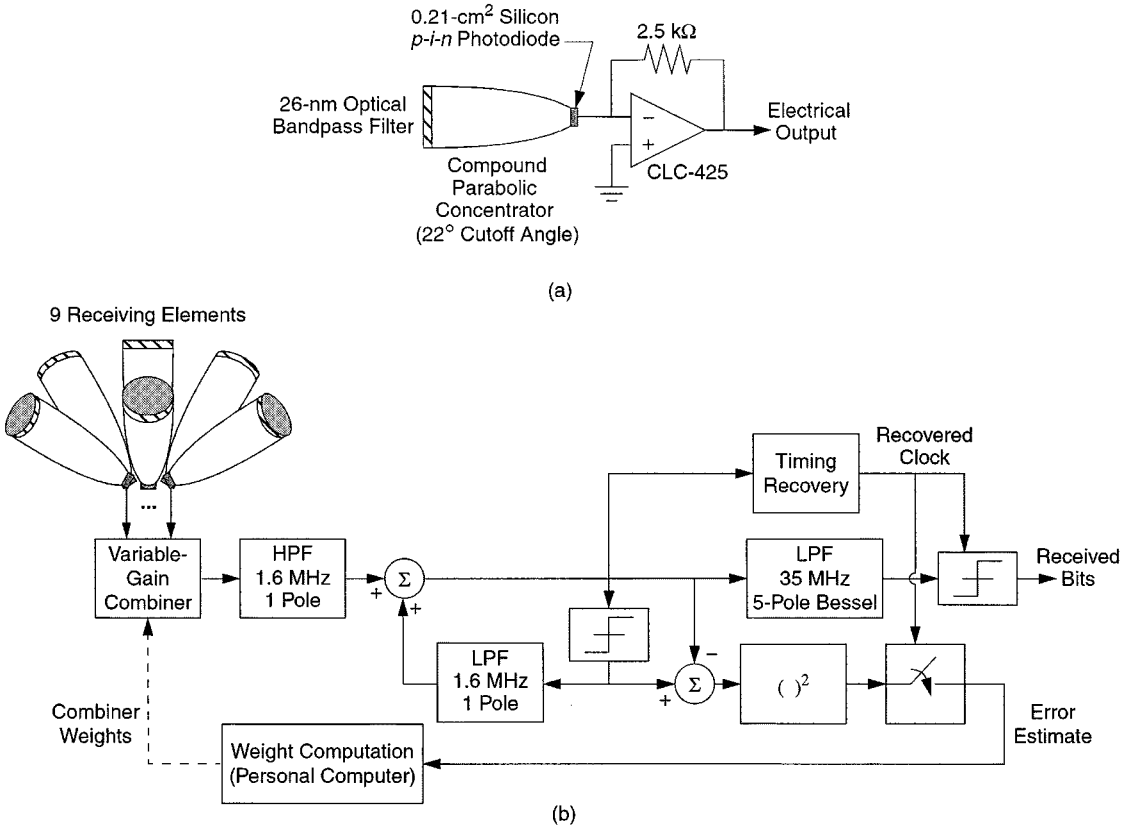

Fig. 11. Experimental angle-diversity receiver. (a) A single optical receiving element. (b) Overall system.

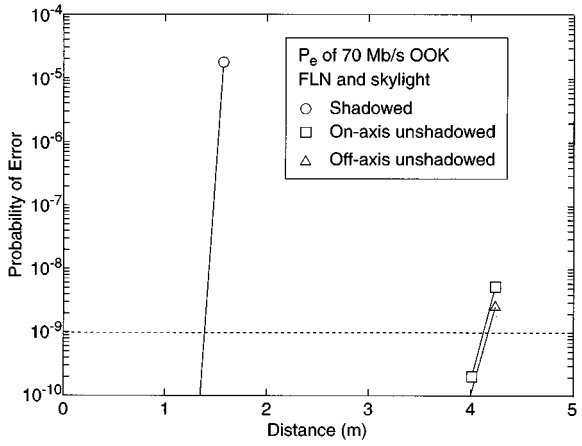

Fig. 12. Probability of error as a function of receiver-to-transmitter distance along room diagonal in the room depicted in Fig. 10(a). Fluorescent light and bright skylight from two windows are present. The bit rate is 70 Mb/s, and OOK is employed.

spreads of the other channels range from 9 ns to 11 ns. Delay spread can also be estimated through the ISI power penalty and the 3-dB frequency, both of which have strong dependence upon delay spread. Both of these estimates imply that the actual delay spread of the first channel is 1.0 ns.

C. Range and Error Performance

Probability of error as a function of distance is shown in Fig. 12. The range achieved at 70 Mb/s is 4.2 m, and is independent of orientation angle of the receiver. Bright sunlight and fluorescent lights were both present in this test, but the measured P_e curves with the sun blocked and fluorescent lights are essentially the same as those shown. Shadowing was done as in [14], by placing a human figure 30 cm away from the receiver in the direction of the transmitter. The performance with shadowing could be improved by providing additional spreading of the transmit beams and by increasing the elevation angle of the receivers, but this would result in a reduction in the unshadowed range.

Probability of error versus received irradiance for SC, EGC, and MRC is shown in Fig. 13. MRC increases the sensitivity by 1 dB over SC and by 2 dB over EGC. In the presence of bright skylight, EGC would perform even more poorly.

V. Conclusions

Multiple transmit beams and narrow FOV receiver elements can improve the performance of nondirected wireless IR links. This performance improvement is due to the reduction in background noise and from reduced multipath distortion in such systems. The improvement is manifested in all of the metrics considered here—reduced delay spread, increased SNR, increased power margin for room coverage, and increased range.

Vertically oriented systems are ideal at high data rates when range is the primary consideration. They are best suited when LOS links are apt to be blocked. They are also useful in very large rooms where one cannot cover the entire room with a single transmitter and so one would need to use multiple transmitters in a cellular pattern. The rapid drop in SNR that these

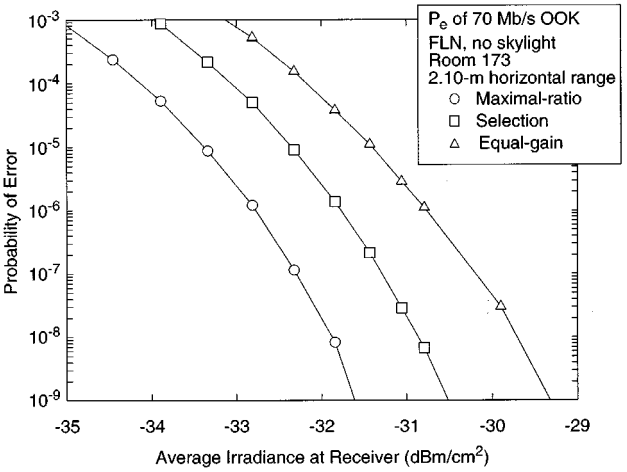

Fig. 13. Probability of error as a function of the average irradiance at the receiver, in the room depicted in Fig. 10(b), which also shows the location of the transmitter "t" and receiver "R." The room has bright fluorescent lights and no skylight.

systems exhibit is a benefit in this context as intercell interference will be reduced. The horizontally oriented systems, which employ multiple directed horizontal beams, provide the best power margin for covering medium-sized rooms. However, they rely on an LOS path for successful operation.

The prototype nondirected IR system achieves a 4.2-m range at 70 Mb/s. The improvements in performance predicted by analysis are also exhibited by this prototype, and the method for parametric estimation of the combiner tap weights with low-complexity hardware implementation was successfully demonstrated.

The primary problem with the receivers described in this paper is the size of the optical elements required, although alternative concentrators exist [17] that have better size versus gain characteristics. Another possible approach would be to use a single lens-based imaging receiver [5] rather than a collection of separate nonimaging concentrators.

REFERENCES

[1] J. M. Kahn and J. R. Barry, "Wireless infrared communications," *Proc. IEEE*, vol. 85, pp. 265–298, Feb. 1997.

[2] J. M. Kahn, W. J. Krause, and J. B. Carruthers, "Experimental characterization of nondirected indoor infrared channels," *IEEE Trans. Commun.*, vol. 43, pp. 1613–1623, Feb./Mar./Apr. 1995.

[3] C. R. A. T. Lomba, R. T. Valadas, and A. M. de Oliveira Duarte, "Sectored receivers to combat the multipath dispersion of the indoor optical channel," in *Proc. IEEE Sixth Int. Symp. on Personal, Indoor and Mobile Radio Communications*, Toronto, ON, Canada, Sept. 1995, pp. 1090–1095.

[4] R. T. Valadas and A. M. de Oliveira Duarte, "Sectored receivers for indoor wireless optical communication systems," in *Proc. IEEE 5th Int. Symp. on Personal, Indoor, and Mobile Radio Communications*, The Hague, The Netherlands, Sept. 1994, pp. 321–325.

[5] P. Djahani and J. M. Kahn, "Analysis of infrared links employing multi-beam transmitters and imaging diversity receivers," in *Proc. IEEE Int. Conf. on Global Communications*, Rio de Janeiro, Brazil, Dec. 1999, pp. 497–504.

[6] G. D. Forney Jr., "Maximum-likelihood sequence estimation of digital sequences in the presence of intersymbol interference," *Proc. IEEE*, vol. 60, pp. 363–378, May 1972.

[7] J. B. Carruthers, "Multipath Channels in Wireless Infrared Communications: Modeling, angle diversity and estimation," Ph.D. dissertation, Univ. of California, Berkeley, Dec. 1997.

[8] E. A. Lee and D. G. Messerschmitt, *Digital Communication*, 2nd ed. Boson, MA: Kluwer, 1994.

[9] J. R. Barry, *Wireless Infrared Communications*. Boston, MA: Kluwer, 1994.

[10] W. Welford and R. Winston, *High Collection Nonimaging Optics*. New York: Academic, 1989.

[11] K.-P. Ho and J. M. Kahn, "Compound parabolic concentrators for narrow-band wireless infrared receivers," *Opt. Eng.*, vol. 34, pp. 1385–1395, May 1995.

[12] J. R. Barry, J. M. Kahn, W. J. Krause, E. A. Lee, and D. G. Messerschmitt, "Simulation of multipath impulse response for indoor wireless optical channels," *IEEE J. Select. Areas Commun.*, vol. 11, pp. 367–379, Apr. 1993.

[13] J. B. Carruthers and J. M. Kahn, "Modeling of nondirected wireless infrared channels," *IEEE Trans. Commun.*, vol. 45, pp. 1260–1268, Oct. 1997.

[14] G. W. Marsh and J. M. Kahn, "Performance evaluation of experimental 50-Mb/s diffuse infrared wireless link using on-off keying with decision-feedback equalization," *IEEE Trans. Commun.*, vol. 44, pp. 1496–1504, Nov. 1996.

[15] T. D. Nguyen, "Receiver Design for Infrared Wireless Communications Systems," M.S. thesis, Univ. of California, Berkeley, July 1995.

[16] R. Narasimhan, M. D. Audeh, and J. M. Kahn, "Effect of electronic-ballast fluorescent lighting on wireless infrared links," *Proc. Inst. Elect. Eng.—Optoelectronics*, vol. 143, pp. 347–354, Dec. 1996.

[17] X. Ning, R. Winston, and J. O'Gallagher, "Dielectric totally internally reflecting concentrators," *Appl. Optics*, vol. 26, pp. 300–305, Jan. 1987.

Jeffrey B. Carruthers (S'87–M'97) received the B.Eng. degree in computer systems engineering from Carleton University, Ottawa, ON, Canada, in 1990, and the M.S. and Ph.D. degrees in electrical engineering from the University of California, Berkeley, in 1993 and 1997, respectively.

He is an Assistant Professor in the Department of Electrical and Computer Engineering at Boston University, Boston, MA. He joined a SONET Development Group of Bell-Northern Research, Ottawa, ON, Canada, in 1990. From 1992 to 1997, he was a Research Assistant at the University of California, Berkeley. In September 1997, he assumed his current position as an Assistant Professor at Boston University. His research interests include wireless networks, wireless communications, and optical communications.

Dr. Carruthers is a recipient of a National Science Foundation CAREER Award, a University of California, Berkeley Regents' Fellowship, and a Natural Sciences and Engineering Research Council of Canada "1967" Scholarship. He is a member of the IEEE Communications Society, the IEEE Information Theory Society, and the IEEE Lasers and Electro-Optics Society.

Joseph M. Kahn (M'87–SM'98–F'00) received the A.B., M.A. and Ph.D. degrees in physics from the University of California, Berkeley, in 1981, 1983 and 1986, respectively.

He is a Professor and Vice Chair for Graduate Matters in the Department of Electrical Engineering and Computer Sciences at the University of California, Berkeley. From 1987 to 1990, he was a Member of Technical Staff in the Lightwave Communications Research Department of AT&T Bell Laboratories, where he performed research on multigigabit-per-second coherent optical fiber transmission systems and related technologies. He joined the faculty of U.C. Berkeley in 1990. His current research addresses several areas of communications, including wireless communication using antenna arrays, wireless communication for microelectromechanical systems (MEMS), optical wireless communication, and optical fiber communications.

Prof. Kahn received the National Science Foundation Presidential Young Investigator Award in 1991. He is a member of the IEEE Communications Society, the IEEE Information Theory Society, and the IEEE Lasers and Electro-Optics Society. He is serving currently as a Technical Editor of *IEEE Personal Communications Magazine*.